ELSEVIER

Journal of Electron Spectroscopy and Related Phenomena 106 (2000) 187–197

JOURNAL OF ELECTRON SPECTROSCOPY and Related Phenomena

www.elsevier.nl/locate/elspec

Pump-probe spectroscopy of ultrafast structural relaxation of electronically excited rare gas heteroclusters

Andreas Heidenreich*, Joshua Jortner

School of Chemistry, Tel Aviv University, Tel Aviv 69978, Israel

Abstract

We advance an approach for the study of multistate dynamics of low Rydberg excitations in $XeAr_N/Xe^*(^3P_1)Ar_N/Xe^+Ar_N$ clusters on the time scale of nuclear motion, as explored by pump-probe neutral-to excited-to positive ion (NEEXPO) femtosecond spectroscopy. The dynamics of the Xe^*Ar_N ($N=54$) cluster induced by charge expansion inferred from the calculation of NEEXPO signals at different probe energies, manifests the lifetime $\tau_1 \simeq 100$ fs for the initial formation of the 'bubble', an intracluster vibrational energy redistribution (IVR) lifetime $\tau_{1/e} \simeq 5.0$ ps and an IVR completion time $\tau_c \simeq 8–10$ ps, which corresponds to the bubble equilibration.

1. Introduction

Ultrafast cluster nuclear dynamics occurring on the time scale of nuclear motion manifests dynamic cluster size effects:

1. Exhibition of a continuous variation of the number of degrees of freedom and the density of states with increasing the cluster size [1,2].
2. Allowance for the separation of time scales between high-frequency (intramolecular) and low-frequency (intermolecular) nuclear dynamics, concurrently with the manifestation of the cluster size dependence of the two times scales [3,4].
3. Establishment of the nature and of the time scales for distinct individual processes of nuclear dynamics, i.e., configurational relaxation, onset of intracluster vibrational energy redistribution (IVR) and possible vibrational equilibration occurring in clusters of variable size [4–6].
4. Exploration of the 'transition' from resonant to dissipative IVR dynamics with increasing the cluster size [4–6].
5. Vibrational coherence effects in nuclear dynamics, their induction mechanisms and information content [5–7].
6. Cluster temperature effects on nuclear dynamics of JVR [points (3) and (4)] and vibrational coherence [point (5)]) [5,6].

Novel features of ultrafast cluster nuclear dynamics can be triggered by charge separation, localization and expansion. Typical examples involve: (a) multistate nuclear dynamics in the $Ag_3^-/Ag_3/Ag_3^+$ negative ion to neutral to positive ion (NENEPO) spectroscopy of small clusters [5,6,8,9], (b) structural relaxation in extravalence electronic Rydberg excitations of Xe^*Ar_N clusters [with $Xe^* \equiv Xe(^3P_1)$], which result in 'bubble' formations around the excited state for the Xe interior sites in medium-sized and large clusters, i.e., $N \sim 54–200$ in theory [7,10] and $N = 100–1.5\times10^5$ in experiment [11,12], and (c) relaxation of an excess electron via the formation of a large 'bubble' (bubble radius $\approx 14–17$ Å) in huge clusters

*Corresponding author.

0368-2048/00/$ – see front matter
PII: S0368-2048(99)00076-6

$(^4He)_N$ or $(^3He)_N$ with $N \geq 10^5$ [13,14]. The two types of 'bubbles' involving configurational relaxation around a charge expanded center of an impurity Rydberg excitation in a rare-gas cluster (type b) or of an excess electron in a large He cluster (type c), originate from strong short-range Rydberg-medium or electron-medium repulsive interactions, which give rise to a large configurational dilation.

Dynamics and the time scale of nuclear motion triggered by vertical electronic- vibrational ionization or excitation can be interrogated by pump-probe spectroscopy. This is the case for the transition state spectroscopy and nuclear dynamics of small clusters induced by photodetachment and explored by NENEPO spectroscopy, which was advanced and investigated both experimentally [8,9] and theoretically [5,6]. It will be of considerable interest to adopt similar methods to explore nuclear dynamics on the time scale of nuclear motion induced by Rydberg excitation, i.e., charge expansion in medium-sized and large Xe^*Ar_N clusters. Molecular dynamics (MD) studies [7] of structural relaxation dynamics of Xe^*Ar_N clusters specified the configurational and temporal parameters for the 'bubble' formation, i.e., large configurational dilation around Xe* for Xe interior sites. The bubble formation for the central Xe site is characterized by a multimodal time evolution, accompanied by vibrational coherence effects, with a short (Gaussian) component ($\tau_0 \simeq 150$ fs) followed by a larger exponential decay component ($\tau_{1/e} \simeq 2$ ps), with the bubble reaching its equilibrium after ≈ 10 ps with an asymptotic spatial expansion of 0.7–0.8 Å. These MD results [7] have to make contact with experimental reality. Goldberg and Jortner [7] attempted to make contact between the MD simulation results and fs time-resolved emission spectroscopy from the Xe^*Ar_N clusters, where experimental study constitutes a difficult challenge. We propose an alternative approach to the nuclear dynamics of Xe^*Ar_N clusters, which rests on the utilization of pump-probe spectroscopy of the three electronic states system, i.e., the neutral ground state $Xe–Ar_N$, the excited state Xe^*Ar_N and the ionic state Xe^+Ar_N, with the structural relaxation dynamics in the Xe^*Ar_N state initially prepared by the vertical excitation being interrogated by a delayed ionization pulse, using the methods of photoelectron spectroscopy. These NEEXPO (neutral-to excited-to ionic cluster) experiments will provide information on the time scale for the 'bubble' formation, IVR and its completion, as well as on vibrational coherence effects induced by charge expansion in rare-gas heteroclusters.

2. Methodology

2.1. Simulations of pump-probe signals

Our pump-probe simulations of NEEXPO signals involve the potential energy hypersurfaces of the ground electronic state ($^1S_0$) of the neutral $XeAr_N$ cluster, its electronically excited $^3P_1$ hypersurface and the hypersurfaces of the $XeAr_N^+$ cation. Due to spin-orbit and crystal field splitting, three low lying doubly degenerate cationic states are involved. In what follows, we shall label the $^1S_0$ energy surface as 0, the $^3P_1$, as 1, and the three cationic surfaces by 2, 3 and 4. We shall simulate the total $Xe–Ar_N^+$ ion current, as it is common in pump-probe experiments not to discriminate the cation yield according to the kinetic energy of the photodetached electrons [5,6,8,9].

We have utilized the Wigner representation of the density matrix introduced by Li et al. [15] to simulate the pump-probe signal. In this classical method, which rests on trajectory calculations, the signal intensity S as a function of the pump-probe delay time t_d is given by [5,6,15,16]

$$S[t_d] \sim \int dq_0 dp_0 \int_0^\infty d\tau_1 \exp\left\{ -\frac{(\tau_1 - t_d)^2}{\sigma_{pu}^2 + \sigma_{pr}^2} \right\} \times \sum_{j=2}^{4} \int_0^\infty dE_2 \exp\left\{ -\frac{\sigma_{pr}^2}{\hbar^2} [E_{pr} - V_{j1}(\boldsymbol{q}_1(\tau_1; q_0)) - E_2]^2 \right\} \times \exp\left\{ -\frac{\sigma_{pu}^2}{\hbar^2} [E_{pu} - V_{10}(\boldsymbol{q}_0)]^2 \right\} P_{00}(\boldsymbol{q}_0, \boldsymbol{p}_0) \quad (1)$$

$P_{00}(\boldsymbol{q}_0, \boldsymbol{p}_0)$ represents the nuclear phase space density of the thermally equilibrated system on hypersurface 0. P_{00} is obtained by sampling coordinates $\boldsymbol{q}_o$ and momenta $\boldsymbol{p}_0$ along a classical trajectory. The sampled

phase space points serve then as the initial conditions for the classical propagation on hypersurface 1, being weighted by the pump transition probability ('spectral filtering'), which is given by the third exponential term in Eq. (1). E_{pu} and σ_{pu} are the excitation energy and the pulse duration of the Gaussian pump laser pulse, respectively, and $V_{10}(q_0)$ is the vertical energy gap of the two hypersurfaces for the given phase space point. After the propagation of the phase space points on energy surface 1 up to time τ_1, the probe transition probability is calculated for the nuclear configuration $\boldsymbol{q}_1(\tau_1)$. This is expressed by the second exponential of Eq. (1) with V_{j1} $(2 \leq j \leq 4)$ being the instantaneous vertical energy gaps, E_{pr} the probe one-photon excitation energy, and σ_{pr} the Gaussian pulse duration. The photo-detached electron can carry away any excess energy above the ionization threshold in terms of kinetic energy. This is taken into account by integrating the spectral intensity over all possible excess energies E_2, where we have assumed a constant density of continuum states for the electron. The probe signal intensity is summed over all the three ionizations $j = 2$–4. The propagation times τ_1 on surface 1 are smeared out because of the finite duration of the pump and probe laser pulse. Accordingly, one has to integrate over all possible propagation times τ_1; the times τ_1 are weighted by the pump-probe correlation function, which is the first exponential in Eq. (1). The outer double integral over $\boldsymbol{q}_0$ and $\boldsymbol{p}_0$ originates from the averaging over all sampled phase space points $(\boldsymbol{q_0}, \boldsymbol{p_0})$ on energy surface 0. The pump energy of $\approx$8.9 eV can be achieved either by a one-photon or by a multiphoton (three-photon) process. In Eq. (1) we have assumed implicitely a non-resonant character of the pump step. However, in our simulations reported in this paper we have not yet incorporated the spectral filtering; σ_{pu} has been set to zero, so that the entire line shape for the $0 \rightarrow 1$ transition is excited. The probe step was simulated for $\sigma_{pr} = 100$ fs.

2.2. Potential energy hypersurfaces

The potential energy hypersurfaces for the ground state $^1S_0$ of $XeAr_N$ and of the extravalence excitation $Xe^*(^3P_1)Ar_N$ were constructed from the superposition of pairwise potentials. For the $XeAr_N^+$ potential surfaces the diatomics in molecules (DIM) method, outlined below, was utilized. For the $^1S_0$ state, Lennard–Jones 6–12 pair potentials were used for the Xe–Ar and for the Ar–Ar interactions. The parameters are: $\sigma_{Xe-Ar} = 3.65$ Å, $\epsilon_{Xe-Ar} = 0.0153$ eV, $\sigma_{Ar-Ar} = 3.405$ Å, and $\epsilon_{Ar-Ar} = 0.0103$ eV [17–19]. For the Xe* $(^3P_1)$ – Ar $(^1S_0)$ interactions, the following exp-6 potential was employed

$$V_{Xe^*-Ar}(R) = \epsilon(1 - 6/\alpha)^{-1} \times \{(6/\alpha)\exp[\alpha(1 - R/R_e)] - (R_e/R)^6\} \quad (2)$$

with the parameters $\epsilon = 0.008$ eV, $R_e = 4.65$ Å, and $\alpha = 15$ [20–22].

A simple pairwise potential cannot give all the low-lying cationic states simultaneously involved in the probe step. Therefore, we have utilized the semiempirical DIM method [23–27]. In several papers the DIM method has been applied to homonuclear rare gas cluster cations Rg_N^+ [28–31], to the $NeHe_2^+$ heteronuclear rare gas cluster [32], and to valence isoelectronic mixed halogen–rare gas clusters [33,34]. In this paper we shall mainly follow the approach of Kuntz et al. [28] and extend the formalism by the inclusion of spin-orbit coupling. The electronic part of the Hamiltonian operator of the n-atomic system is

$$\hat{H} = \sum_{A=1}^{n}\sum_{B=A+1}^{n}(\hat{H}_{AB}) - (n-2)\sum_{A=1}^{n}(\hat{H}_A) + \hat{V}_{SO} \quad (3)$$

The first two terms of Eq. (3) represent the usual partition of the Hamiltonian into diatomic and atomic fragments AB and A, respectively, and the third term expresses the spin-orbit coupling. The ansatz for the total wavefunction $|\Psi_i\rangle$ is a linear combination of Slater determinants $|\Phi_\mu\rangle$ of $M_S = \pm 1/2$

$$|\Psi_i\rangle = \sum_\mu (c_{\mu i}|\Phi_\mu\rangle). \quad (4)$$

The Slater determinants $|\Phi_\mu\rangle$ are built up from atomic spin orbitals consisting of the Cartesian p_x, p_y, p_z orbitals of α and β spin. This implies that for a given Slater determinant the corresponding atomic fragments are either in an ^1S or in an ^2P electronic state. Consequently, the dimension of each Slater

determinant of a $XeAr_N^+$ cation is $6N+5$. The dimension of the Hamiltonian matrix is $6N+6$, as the hole can be located in any of the $6N+6$ spin orbitals.

The basic approximation of the DIM method, which is crucial for reducing the calculation of matrix elements to known diatomic and atomic energies, is that the wave function, Eq. (4), is assumed to be an eigenfunction of the atomic and diatomic fragments. The approximative nature of this assumption is a consequence of the finiteness of the DIM basis, in particular the lack of higher excited electronic configurations. For the DIM basis (4) the eigenvalue equations read:

$$\hat{H}_{AB}(c_{1j}|\Phi_\mu^A\rangle + c_{2j}|\Phi_\nu^B\rangle) = E_j(c_{1j}|\Phi_\mu^A\rangle + c_{2j}|\Phi_\nu^B\rangle) \tag{5}$$

$$\hat{H}_{AB}|\Phi_\mu^C\rangle = E_{AB}|\Phi_\mu^C\rangle \tag{6}$$

$$\hat{H}_A|\Phi_\mu^A\rangle = E_{A^+}|\Phi_\mu^A\rangle \tag{7}$$

$$\hat{H}_A|\Phi_\mu^C\rangle = E_A|\Phi_\mu^C\rangle \tag{8}$$

$|\Phi_\mu^A\rangle$, $|\Phi_\mu^B\rangle$, and $|\Phi_\mu^C\rangle$ are the Slater determinants, which correspond to a hole in orbital μ on atom A, B, and C, respectively. Eq. (5) represents the case in which the hole is located at the same diatomic fragment AB as the diatomic Hamiltonian $\hat{H}_{AB}$. In this case the eigenfunction is taken to be a linear combination of two Slater determinants, in which the hole is located at atoms A and B, respectively. Eq. (6) applies when the hole is at any atom C not being part of the diatomic fragment AB. The eigenvalue E_{AB} is the energy of the neutral AB fragment. The eigenvalues of the atomic eigenvalue Eqs. (7) and (8) are the ionization energy E_{A+} or the energy E_A of the neutral atom, respectively, depending whether the hole is located on atom A or on any other atom C.

Let $\{\Phi_x^A, \Phi_y^A, \Phi_z^A, \Phi_x^B, \Phi_y^B, \Phi_z^B\}$ be the Slater determinants of the entire cationic cluster with the hole in a p_x, p_y, p_z orbital being located at atoms A or B (the spin is disregarded for the time being). The diatomic fragment Hamiltonian $\hat{H}_{AB}$ on this basis reads

$$H_{AB} = \begin{bmatrix} \Pi_{AA} & 0 & 0 & \Pi_{AB} & 0 & 0 \\ 0 & \Pi_{AA} & 0 & 0 & \Pi_{AB} & 0 \\ 0 & 0 & \Sigma_{AA} & 0 & 0 & \Sigma_{AB} \\ \Pi_{AB} & 0 & 0 & \Pi_{BB} & 0 & 0 \\ 0 & \Pi_{AB} & 0 & 0 & \Pi_{BB} & 0 \\ 0 & 0 & \Sigma_{AB} & 0 & 0 & \Sigma_{BB} \end{bmatrix} \tag{9}$$

where the AB interatomic axis defines the z axis (local coordinate system). The matrix elements Σ_{AA}, Σ_{AB}, Σ_{BB} of the Σ states and Π_{AA}, Π_{AB}, Π_{BB} of the Π states are obtained from inverting the following 2×2 eigenvalue problem

$$\begin{pmatrix} c_{11} & c_{21} \\ c_{12} & c_{22} \end{pmatrix}\begin{pmatrix} H_{AA} & H_{AB} \\ H_{AB} & H_{BB} \end{pmatrix}\begin{pmatrix} c_{11} & c_{12} \\ c_{21} & c_{22} \end{pmatrix} = \begin{pmatrix} E_1 & 0 \\ 0 & E_2 \end{pmatrix} \tag{10}$$

Therein, H_{AA}, H_{AB} and H_{AB} represent either Σ_{AA}, Σ_{AB}, Σ_{BB} or Π_{AA}, Π_{AB}, Π_{BB}. Eq. (10) follows from the eigenvalue Eq. (5), neglecting diatomic overlap. E_1 and E_2 are the eigenvalues of the $1^2\Sigma$ and $2^2\Sigma$ or $1^2\Pi$ and $2^2\Pi$ states, respectively, which are taken from ab initio CI calculations. The eigenvector coefficients are derived from the corresponding Mulliken charges of the CI vectors, taking opposite signs of the coefficients for the linear combination $c_{11}|\Phi_\mu^A\rangle + c_{21}|\Phi_\nu^{B\prime}\rangle$ of the lowest Σ state (because of the relative orientation of the p_σ orbitals) and equal signs for the lowest Π state. When setting up the Hamiltonian matrix of the entire system, the diatomic matrix H_{AB}, Eq. (9), has to be transformed from the local (diatomic) to the global coordinate system [28]. For the other matrix elements one obtains

$$\langle\Phi_\mu^C|\hat{H}_{AB}|\Phi_\mu^C\rangle = E_{AB}, (\{C,D\}\neq\{A,B\}) \tag{11}$$

$$\langle\Phi_\mu^C|\hat{H}_{AB}|\Phi_\nu^A\rangle = \langle\Phi_\mu^C|\hat{H}_{AB}|\Phi_\lambda^D\rangle = 0(\{C,D\}\neq\{A,B\}) \tag{12}$$

$$\langle\Phi_\mu^A|\hat{H}_A|\Phi_\mu^A\rangle = E_A^+ \tag{13}$$

$$\langle\Phi_\mu^C|\hat{H}_A|\Phi_\mu^C\rangle = E_A \tag{14}$$

$$\langle\Phi_\mu^C|\hat{H}_A|\Phi_\mu^A\rangle = \langle\Phi_\mu^C|\hat{H}_A|\Phi_\lambda^D\rangle = 0 \tag{15}$$

In the treatment of the spin-orbit coupling [35–37] adopted in this work only matrix elements $\langle \Phi^{A}_{\mu} | \hat{V}_{SO} | \Phi^{A}_{\nu} \rangle$ of Slater determinants with the hole being located at the same atom are considered; the matrix representation of $\hat{V}_{SO}$ in the entire DIM basis, Eq. (4), is block diagonal. In the basis of Slater determinants $\{\Phi^{A}_{x\alpha}, \Phi^{A}_{y\alpha}, \Phi^{A}_{z\alpha}, \Phi^{A}_{x\beta}, \Phi^{A}_{y\beta}, \Phi^{A}_{z\beta}\}$ (i.e., the hole being located in the $p_x\alpha$, $p_y\alpha$ etc. spin orbitals) a diagonal block matrix V^{A}_{SO} is given (in atomic units) by

$$V^{A}_{SO} = \frac{\Delta_A}{3} \begin{pmatrix} 0 & -i & 0 & 0 & 0 & -1 \\ i & 0 & 0 & 0 & 0 & i \\ 0 & 0 & 0 & -1 & i & 0 \\ 0 & 0 & -1 & 0 & i & 0 \\ 0 & 0 & i & -i & 0 & 0 \\ 1 & -i & 0 & 0 & 0 & 0 \end{pmatrix}. \quad (16)$$

Δ_A is the spin-orbit splitting constant of the isolated Xe^+ (1.31 eV) or of the Ar^+ (0.18 eV) cation [38]. Δ_A is assumed to be unaltered in the cluster and to be independent of the interatomic distances.

The quantum chemistry calculations for the lowest state for Xe–Ar^+ ($1^2\Sigma^+$) and Ar_2^+ ($1^2\Sigma_u^+$) were carried out at the CCSD(T)/VQZ* level, i.e., by performing coupled cluster calculations involving singly, doubly and triply excited configurations without including the triply excited configurations into the iterations [39], and using the quadruple-ζ basis set of Nicklass et al. [40]. The configurations were generated from the UHF (unrestricted Hartree–Fock) MOs of the cations. The basis set uses relativistic effective core potentials (ECP) to replace 46 inner shell electrons of Xe and 10 of Ar. The polarization functions consist of three sets of d functions and one set of f functions per atom. The CCSD(T) calculations were carried out employing the GAUSSIAN94 program package [41]. Since the GAUSSIAN94 code allows only for calculating the lowest eigenstate, the excited states were obtained at the SDCI/VQZ* level (singly and doubly excited configuration interaction) using the GAMESS(US) program package [42]. The configurations were generated from the RHF (restricted Hartree–Fock) MOs of the neutral XeAr and Ar_2. The reference configuration consisted of seven doubly and one singly occupied MO. For XeAr+ the virtual space was limited to 51 orbitals, and the uppermost 29 virtual orbitals were kept frozen. For Ar_2^+ the virtual space consisted of 62 orbitals, and the remaining 18 virtual orbitals were kept frozen.

The distance dependent eigenvalues E_1 and Mulliken charges were interpolated from the sampled points using a cubic spline algorithm. Each sampled eigenvalue was processed in the following way

$$E_j(R) = E_{j,CI}(R) - E_{j,CI}(R \to \infty) + E_{A^+,exp}. \quad (17)$$

$E_{j,CI}(R)$ and $E_{j,CI}(R \to \infty)$ are the ab initio CI eigenvalues at distance R and at 'infinite' (20 Å) distance, respectively, and $E_{A^+,exp}$ is the experimental ionization energy of atom A. $E_{A^+,exp}$ is taken at the center of the multiplet. Since the experimental ionization energies refer to the $^2P_{3/2}$ component (Xe: 12.127 eV, Ar: 15.755 eV [43]), a value of $\Delta/3$ has to be added. Eq. (17) implies that the energies E_A of the neutral atoms in Eq. (14) is set to zero and that their subtraction in the matrix representation of Eq. (3) becomes unnecessary. For E_{AB}, Eq. (11), we take the Lennard–Jones pairwise term of the neutral cluster.

We used a third-order Gear predictor-corrector algorithm to integrate the classical equations of motion [44] with an integration time step of 1 fs. The equilibrium temperature (20 K) $T = 2\langle E_{kin}\rangle/(3n-6)k_B$ ($\langle E_{kin}\rangle$: time-averaged kinetic energy of the nuclei, k_B: Boltzmann constant) of the cluster in the $^1S_0$ electronic state was achieved by an iterative rescaling of the velocities. The sampling interval of the phase space on the $^1S_0$ hypersurface was 40 fs and of the energy gaps, V_{21}, V_{31} and V_{41} 16 fs. The signals were averaged over 500 trajectories.

3. Potential curves for XeAr, Xe*Ar, $XeAr^+$, and Ar_2^+

Fig. 1 shows the XeAr potential curves for the $^1S_0$ and the $^3P_1$ state. The equilibrium distances are 4.10 and 4.60 Å for the $^1S_0$ and for the $^3P_1$ state, respectively, reflecting the larger spatial extension of the electronically excited Xe atom and thus the driving force of the bubble formation. In the $XeAr_{54}$ cluster the equilibrium distances for both electronic states shrink to 3.76 and 4.04 Å, respectively.

The calculated potential curves of the $XeAr^+$

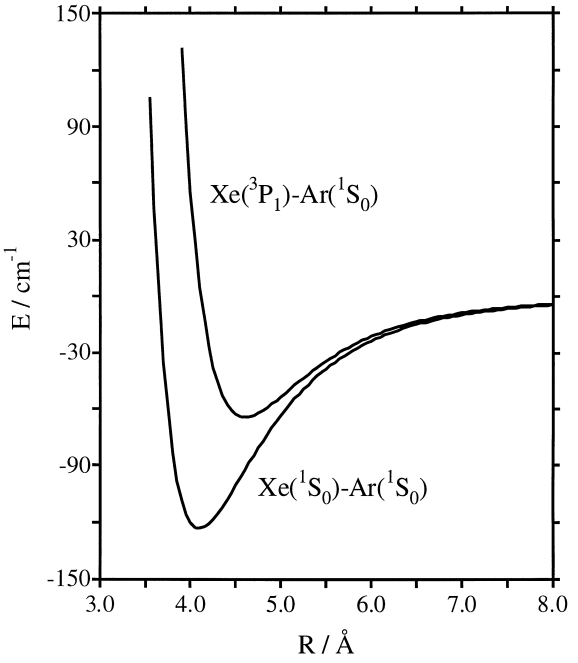

Fig. 1. Xe–Ar diatomic potential curves for the $^1S_0$ (Lennard–Jones 6–12 potential) and for the $^3P_1$ (exp-6 potential) state. For both potentials the dissociation limit is chosen as the origin of the energy axis.

cation without spin-orbit splitting are given in Fig. 2a. In Fig. 2b the spin-orbit splitting is incorporated according to Eq. (16). The equilibrium distances and binding energies are summarized in Tables 1 and 2. Since the probe step involves only the lowest electronic states, in which the hole is almost exclusively localized at the Xe atom, the choice of the $XeAr^+$ diatomic potential is crucial and we shall therefore discuss it somewhat more detailed. The lower three curves of Fig. 2b correspond to the dissociation products $Xe^+ + Ar$, and therefore show the spin-orbit splitting of the Xe^+ ion at larger R, while the upper three curves exhibit the spin-orbit splitting of the Ar^+ ion. Despite of a strong mixing, we have classified the electronic states by Σ and Π according to the dominant character of their eigenvectors. Ng et al. [45] obtained a value of -0.14 ± 0.02 eV for the binding energy of the lowest electronic state of $XeAr^+$, Dehmer et al. obtained a value of -0.176 ± 0.012 eV [46], whereas experimental interatomic equilibrium distances have not been yet determined. Our calculated binding energy of -0.121 eV for the $1^2\Sigma^+_{1/2}$ state (Table 2) is close to the lower limit of Ng et al. [45] and seems to underestimate the experimental value of Ng et al. [45] and Dehmer et al. [46]. There are two mechanisms by which spin-orbit coupling lowers the binding energy of the lowest cationic state. The first one is that the chemical binding causes an increasing energy separation of the $1^2\Sigma$ and the $1^2\Pi$ curves with decreasing interatomic distance R. This effect was reported by Wadt for homonuclear rare gas ions Rg_2^+ [47]. Specifically, for $XeAr^+$ the $1^2\Pi$ curve is less attractive than the $1^2\Sigma$ curve and the equilibrium distance is located at larger R, so that at $\approx$3.0 Å, where the potential curve of the $1^2\Sigma$ state has its minimum, the $1^2\Pi$ curve is already repulsive and the energy separation of the two curves assumes a value of 0.5 eV. The Σ–Π energy separation means that the off-diagonal spin-orbit matrix elements can cause only a smaller splitting around the minimum of the $1^2\Sigma$ curve than for large R. Consequently, the spin-orbit stabilization of the lower electronic state is smaller in the molecular ion than in the isolated Xe^+ ion; the potential curve becomes more shallow and the equilibrium distance is increased from 2.99 to 3.22 Å. In the homonuclear case, the coupling of the $1^2\Sigma^+$ ($^2\Sigma^+_u$) state is restricted by symmetry to the $2^2\Pi$ ($^2\Pi_u$) state. The second effect, which in the present case is much smaller than the first one, is that with decreasing R the hole is partly localized on the Ar atom, experiencing the smaller spin-orbit coupling constant of the Ar atom. Consequently, the energy stabilization by spin-orbit coupling decreases with decreasing R.

At the present stage of our computations two sources of errors of the calculated potential curves seem possible. Despite the good agreement of the SDCI and the CCSD(T) results for the equilibrium distances and binding energies for the lowest Σ state, the SDCI calculations for the excited states might be less accurate. Therefore CCSD(T) calculations are desirable also for the excited states. The other and apparently more likely source of error is the simplified treatment of the spin-orbit coupling, keeping the radial part of the spin-orbit coupling matrix elements independent of the interatomic distance [37].

The potential curves of the Ar_2^+ ion without and with spin-orbit coupling are displayed in Fig. 3, the

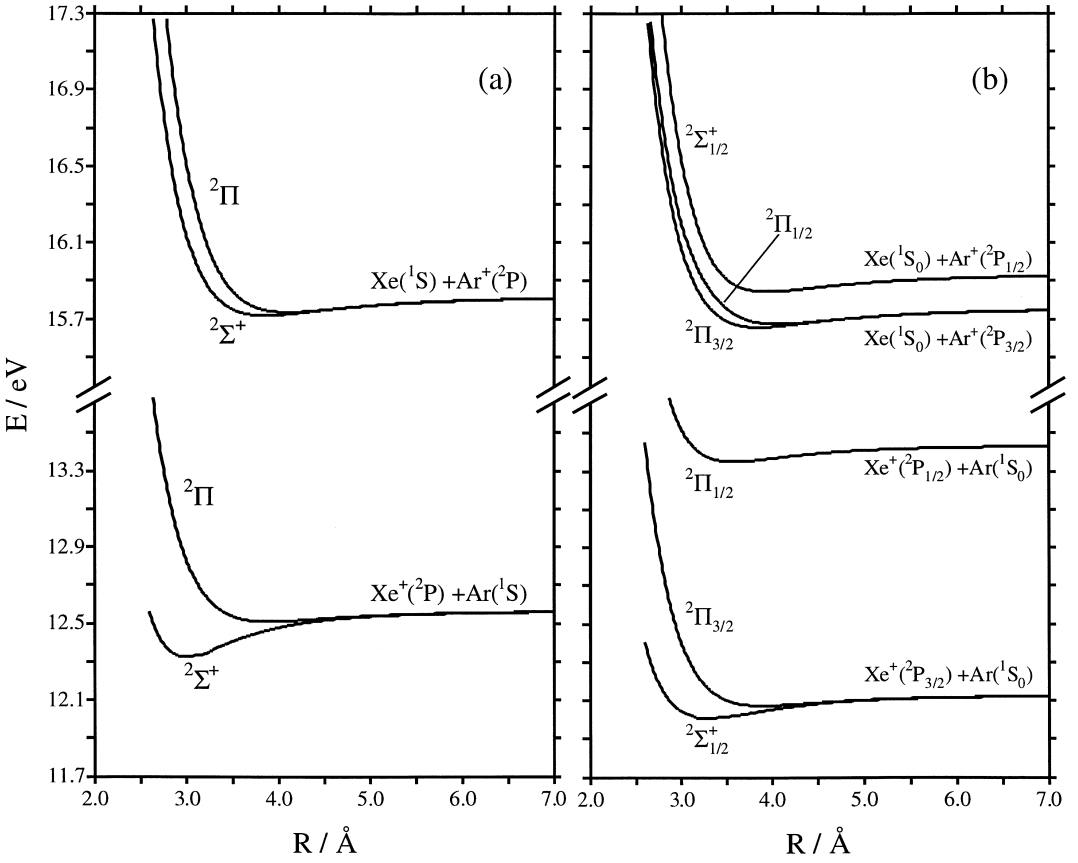

Fig. 2. $XeAr^+$ potential curves (a) without spin-orbit coupling. The $1^2\Sigma^+$ curve was calculated at the CCSD(T), the other potential curves at the SDCI level. The potential curves are shifted in energy according to Eq. (17) such that the dissociation limits coincide with the experimental ionization energies of Xe and Ar (centers of the multiplets); (b) with spin-orbit coupling.

equilibrium distances and binding energies are listed in Tables 1 and 2. For the lowest $^2\Sigma_{3/2u}$, state we obtained a binding energy of -1.21 eV, being in good agreement with the experimental value of -1.269 ± 0.017 eV [48] and with previous calculations of Wadt [47].

The positive atomic charge induces a dipole moment on the surrounding atoms. While the

Table 1
Equilibrium distances and binding energies of the electronic states of the $XeAr^+$ and Ar_2^+ cations without spin-orbit coupling; the results were obtained at the SDCI/VQZ* computational level except for the lowest Σ state, for which the CCSD(T) results are given instead, and the SDCJ values are included in brackets

$XeAr^+$			Ar_2^+		
State	R_e (Å)	E_{Bind} (eV)	State	R_e (Å)	E_{Bind} (eV)
$^2\Sigma^+_{1/2}$	2.99 (3.00)	−0.238 (−0.224)	$^2\Sigma^+_u$	2.42 (2.43)	−1.27 (−1.23)
$^2\Pi$	3.88	−0.055	$^2\Pi_g$	3.10	−0.13
$^2\Pi$	3.85	−0.098	$^2\Pi_u$	4.11	−0.026
$^2\Sigma^+$	4.10	−0.080	$^2\Sigma^+_g$	5.95	−0.0042

Table 2
Equilibrium distances and binding energies of the $XeAr^+$ and Ar_2^+ cations including spin-orbit energies of the electronic states of coupling

$XeAr^+$			Ar_2^+		
State	R_e (Å)	E_{Bind} (eV)	State	R_e (Å)	E_{Bind} (eV)
$^2\Sigma^+_{1/2}$	3.22	−0.121	$^2\Sigma^+_{1/2u}$	2.42	−1.21
$^2\Pi_{3/2}$	3.89	−0.055	$^2\Sigma_{3/2g}$	3.10	−0.134
$^2\Pi_{1/2}$	3.57	−0.086	$^2\Pi_{1/2g}$	4.11	−0.026
$^2\Pi_{3/2}$	3.85	−0.098	$^2\Pi_{3/2u}$	5.24	−0.0068
$^2\Sigma_{1/2}$	4.06	−0.081	$^2\Sigma_{1/2u}$	3.80	−0.061
$^2\Sigma^{+'}_{1/2}$	3.94	−0.091	$^2\Sigma^{+'}_{1/2g}$	4.78	−0.014

diatomic potential curves calculated by the quantum chemistry methods contain the contribution of the polarization to the total energy of the diatomic fragments implicitely, three-body ion–atom–atom charge-induced dipole–dipole interactions are not included. These dipole–dipole interactions will be incorporated in a subsequent work by summing over the contributions of point dipoles [33,49]. First test calculations showed that the dipole–dipole interactions contribute to the total energy by ≈0.1 eV for $XeAr^+_{54}$.

4. Pump-probe signals

Fig. 4 shows a typical example of single-trajectory $^2P_{3/2} - {}^3P_1$ and $^2P_{1/2} - {}^3P_1$ energy gaps for the $XeAr_{54}$ cluster with the Xe atom in the central position. Each of the three energy gap functions corresponds to a doubly degenerate state, the lower two near-degenerate curves to $J = 3/2$ and the upper one to $J = 1/2$, being separated by approximately the spin-orbit coupling constant of Xe^+. The bubble formation causes an increase of the energy gaps of more than 0.5 eV within the first 100 fs after the pump excitation. The subsequent oscillations of the

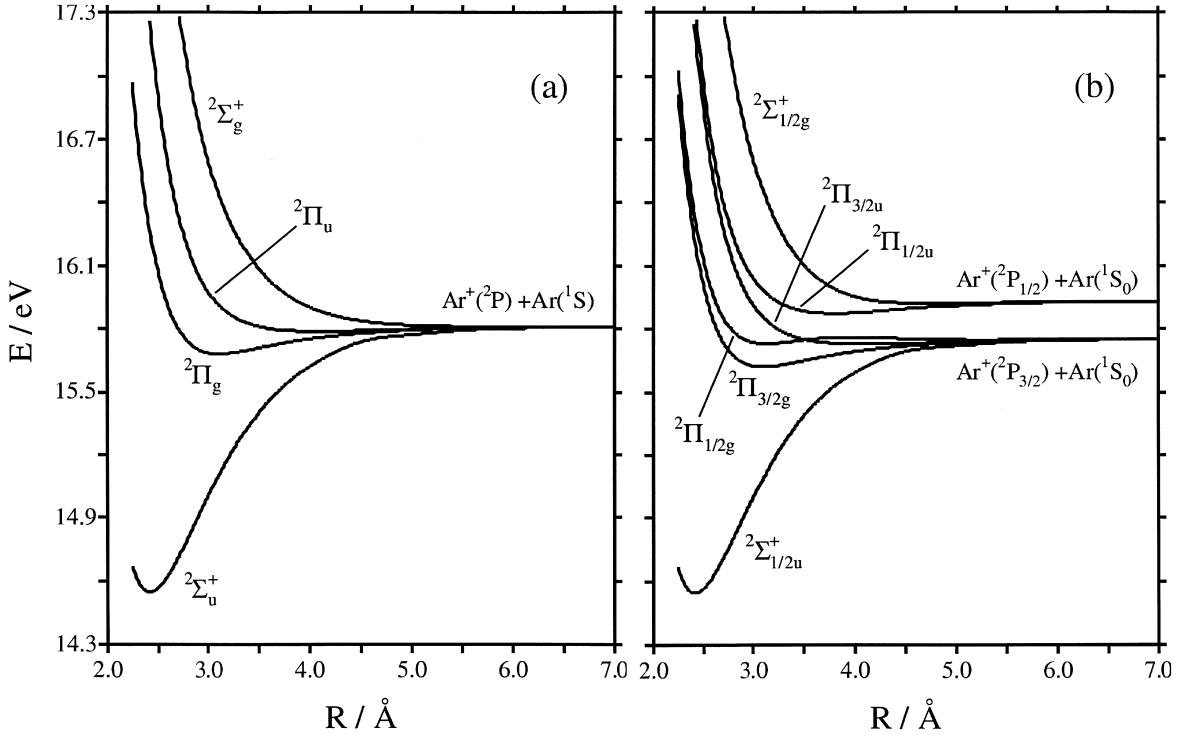

Fig. 3. Ar_2^+ potential curves (a) without spin-orbit coupling. The $1^2\Sigma$ curve was calculated at the CCSD(T), the other potential curves at the SDCI level. The potential curves are shifted in energy according to Eq. (17) such that the dissociation limits coincide with the experimental ionization energy of Ar (center of the multiplet); (b) with spin-orbit coupling.

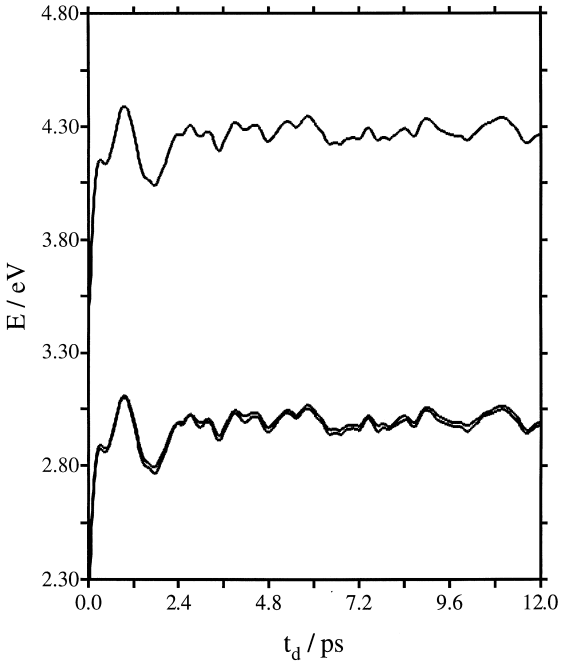

Fig. 4. Energy gaps V_{21}, V_{31}, and V_{41} sampled along a single trajectory of $XeAr_{54}$ (Xe in central position) at the initial temperature of 20 K. The lower two near degenerate energy gap functions correspond to the $J = 3/2$, the upper one to the $J = 1/2$ component.

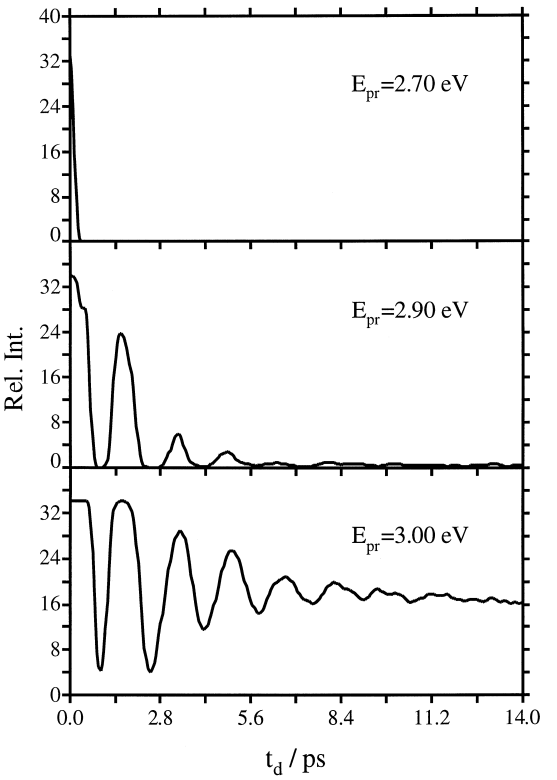

Fig. 5. Simulated pump-probe signals of $XeAr_{54}$ (Xe in central position) for probe energies of 2.7, 2.9 and 3.0 eV and an initial temperature of 20 K.

energy gaps reflect the strong impact induced vibrations in the cluster.

Fig. 5 exhibits the simulated signals for probe energies of 2.7, 2.9 and 3.0 eV. According to Fig. 4 a probe energy of 2.7 eV is sufficient to ionize the cluster only during the initial bubble formation. Consequently, at the probe energy of 2.7 eV the lifetime of the signal of $\tau_I \approx 100$ fs manifests the time scale of the initial bubble formation. The value of $\tau_I \approx 100$ fs is in accord with previous MD simulations [7]. An oscillating signal can be observed, if an energy gap alternately falls below and exceeds a given probe energy E_{pr}. This condition is satisfied for the signals at 2.9 and 3.0 eV. The main frequency component of the vibrational coherence is 20 cm^{-1} for both probe energies. The decay behavior of the oscillations of the signal is probe energy dependent. The decay is non-exponential with $1/e$ times of $\tau_{1/e} = 2.4$ ps and $\tau_{1/e} = 5.0$ ps, and the times when the decay is complete are 6–8 and 8–10 ps for the probe energies of 2.9 and 3.0 eV, respectively. The reason for this dependence of the $1/e$ time and the saturation time of the signal on the probe energy is that the probe signal can experience the damped oscillations of the energy gap for a longer time, when the probe energy is chosen close to the center of the energy gap oscillations, i.e., close to the long-time average value of the energy gap. Consequently, the decay of the oscillatory signal for a single probe energy is not neccessarily equivalent to the IVR time. Instead, only the maximum decay time observed over the entire range of probe energies indicates the completion of IVR, i.e., 5.0 ps and 8–10 ps may be assigned to the $1/e$ and to the time of completion of IVR. The maximal $1/e$ lifetime and the completion time of IVR manifest the dynamic features of the 'bubble' formation in the $XeAr_{54}$ cluster. The completion time obtained from the time-resolved data is in accord with the time ≈ 10 ps for the 'bubble' reaching the equilibrium in the MD simulations [7].

Unlike at $E_{pr} = 2.9$ eV, the signal at 3.0 eV exhibits a notable ion current also for long delay times ($t_d \geq 10$ ps), because the probe energy exceeds the long-time energy gap. At even higher probe energies 3.2–3.5 eV a constant ion current is obtained, which is completely time and probe energy independent, because the probe energy always exceeds the oscillating energy gap values. The signal becomes again time and probe energy dependent in the range $E_{pr} =$ 3.7–4.4 eV, when the energy gap oscillations of the $J = 1/2$ component come into play. The signals at 4.0, 4.2 and 4.3 eV, Fig. 6, exhibit a very similar temporal behavior as their $J = 3/2$ counterparts. The main differences are the constant background ion current caused by the $J = 3/2$ component and the lower intensity of the oscillations due to the fact that the $J = 1/2$ component corresponds only to a single doubly degenerate state. In conclusion, we have advanced a NEEXPO approach for the exploration of the fate of Rydberg states in rare gas heteroclusters. Our predictions will hopefully provide impetus for experimental work in this interesting field.

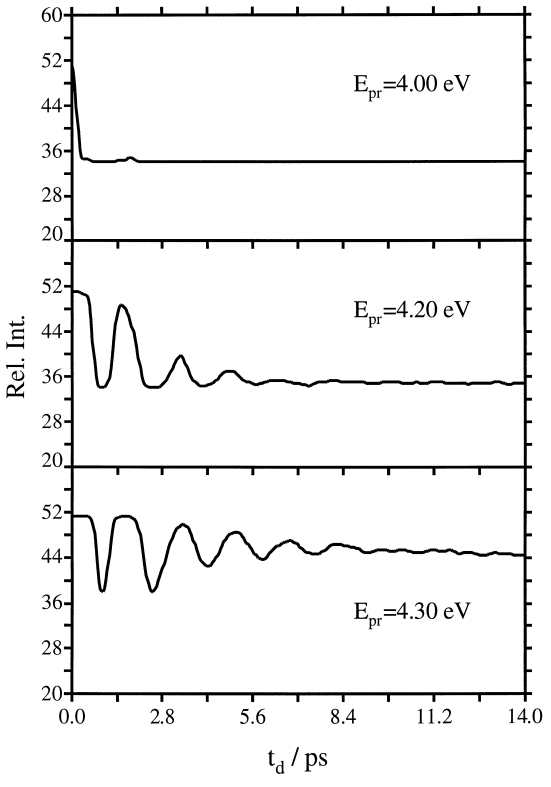

Fig. 6. Simulated pump-probe signals of $XeAr_{54}$ (Xe in central position) for probe energies of 4.0, 4.2 and 4.3 eV and an initial temperature of 20 K.

Acknowledgements

We are grateful to Professor Isidore Last and to Professor Uzi Kaldor for stimulating discussions. We are indebted to the Inter University Computation Center (IUCC) and to the Computation Center at Tel Aviv University for granting computation time and for excellent service. This research was supported by the Volkswagen Foundation and by the Israeli-German binational James-Franck program at Tel Aviv University for laser-matter interaction.

References

[1] J. Jortner, Z. Phys. D. 24 (1992) 247.
[2] J. Jortner, J. Chim. Phys. 92 (1995) 205.
[3] J. Jortner, R.D. Levine, Isr. J. Chem. 30 (1990) 207.
[4] D. Scharf, J. Jortner, U. Landman, J. Chem. Phys. 88 (1988) 4273.
[5] M. Hartmann, J. Pittner, V. Bonačić-Koutecký, A. Heidenreich, J. Jortner, J. Chem. Phys. 108 (1998) 3096.
[6] M. Hartmann, A. Heidenreich, J. Pittner, V. Bonač-Koutecký, J. Jortner, J. Phys. Chem. 102 (1998) 4069.
[7] A. Goldberg, J. Jortner, J. Chem. Phys. 107 (1997) 8994.
[8] S. Wolf, G. Sommerer, S. Rutz, E. Schreiber, T. Leisner, L. Wöste, R.S. Berry, Phys. Rev. Lett. 74 (1995) 4177.
[9] D.W. Boo, Y. Ozaki, L.H. Andersen, W.C. Lineberger, J. Phys. Chem. A. 101 (1997) 6687.
[10] A. Goldberg, A. Heidenreich, J. Jortner, J. Phys. Chem. 99 (1995) 2662.
[11] M. Lengen, M. Joppien, R. Müller, T. Wörmer, T. Möller, Phys. Rev. Lett. 68 (1992) 2362.
[12] R. von Pietrowsky, M. Lengen, L. Moussavizadeh, L. Museur, A.V. Kanaev, M.C. Castex, T. Möller, Faraday Discuss. 108 (1997) 175.
[13] M. Rosenblit, J. Jortner, Phys. Rev. Lett. 75 (1995) 4079.
[14] M. Rosenblit, J. Jortner, J. Phys. Chem. A. 101 (1997) 751.
[15] Z. Li, J.-Y. Fang, C.C. Martens, J. Chem. Phys. 104 (1996) 6919.
[16] M. Hartmann, J. Pittner, H. van Dam, V. Bonačić-Koutecký, Eur. J. Phys. D, in press.
[17] A. Rahman, Phys. Rev. 136 (1964) 405.
[18] L. Verlet, Phys. Rev. 159 (1967) 98.
[19] M.L. Klein, J.A. Venables (Eds.), Rare Gas Solids, Academic, London, 1976.
[20] I. Messing, B. Raz, J. Jortner, J. Chem. Phys. 66 (1977) 2239.

[21] I. Messing, B. Raz, J. Jortner, J. Chem. Phys. 66 (1977) 4577.
[22] I. Messing, B. Raz, J. Jortner, Chem. Phys. 23 (1977) 23.
[23] F.O. Ellison, J. Am. Chem. Soc. 85 (1963) 3540–3544.
[24] J.C. Tully, in: G.A. Segal (Ed.), Modern Theoretical Chemistry, Vol. 7A, Plenum, New York, 1977, p. 173.
[25] J.C. Tully, Adv. Chem. Phys. 42 (1980) 63.
[26] P.J. Kuntz, Ber. Bunsenges. Phys. Chem. 86 (1982) 367.
[27] I. Last, Chem. Phys. 55 (1981) 237.
[28] P.J. Kuntz, J. Valldorf, Z. Phys. D. 8 (1988) 195.
[29] T. Ikegami, T. Kondow, S. Iwata, J. Chem. Phys. 98 (1993) 3038.
[30] T. Ikegami, S. Iwata, J. Chem. Phys. 105 (1996) 10734.
[31] G.A. Morales, J. Faulkner, R.A. Hall, J. Chem. Phys. 109 (1998) 3418.
[32] J. Kendrick, P.J. Kuntz, J. Chem. Phys. 70 (1979) 736.
[33] I. Last, T.F. George, M.E. Fajardo, V.A. Apkarian, J. Chem. Phys. 87 (1987) 5917.
[34] A.I. Krylov, R.B. Gerber, R.D. Coalson, J. Chem. Phys. 105 (1996) 4626.
[35] J.S. Cohen, B. Schneider, J. Chem. Phys. 61 (1974) 3230.
[36] P.J. Hay, T.H. Dunning, R.C. Raffenetti, J. Chem. Phys. 65 (1976) 2679.
[37] P.J. Hay, T.H. Dunning, R.C. Raffenetti, J. Chem. Phys. 66 (1977) 1306.
[38] C.E. Moore, Atomic Energy Levels, Natl. Bur. Stand. Circ. 467, Vol. 1 (1949), Vol. 2 (1952), Vol. 3 (1958).
[39] R.D. Bartlett, in: D.R. Yarkony (Ed.), Modern Electronic Structure Theory, Part II, World Scientific, Singapore, 1995, p. 1047.
[40] A. Nicklass, M. Dolg, H. Stoll, H. Preuss, J. Chem. Phys. 102 (1995) 8942.
[41] Gaussian 94, Revision D.l, M.J. Frisch, G.W. Trucks, H.B. Schlegel, P.M.W. Gill, B.G. Johnson, M.A. Robb, J.R. Cheeseman, T. Keith, G.A. Petersson, J.A. Montgomery, K. Raghavachari, M.A. Al-Laham, V.G. Zakrzewski, J.V. Ortiz, J.B. Foresman, J. Cioslowski, B.B. Stefanov, A. Nanayakkara, M. Challacombe, C.Y. Peng, P.Y. Ayala, W. Chen, M.W. Wong, J.L. Andres, E.S. Replogle, R. Gomperts, R.L. Martin, D.J. Fox, J. S. Binkley, D.J. Defrees, J. Baker, J.P. Stewart, M. Head-Gordon, C. Gonzalez, J.A. Pople, Gaussian, Pittsburgh PA, 1995.
[42] M.W. Schmidt, K.K. Baldridge, J.A. Boatz, S.T. Elbert, M.S. Gordon, J.H. Jensen, S. Koseki, N. Matsunaga, K.A. Nguyen, S.J. Su, T.L. Windus, M. Dupuis, J.A. Montgomery, J. Comput. Chem. 14 (1993) 1347.
[43] K.S. Song, R.T. Williams, Self-Trapped Excitons, Springer, Berlin, 1993.
[44] M.P. Allen, D.J. Tildesley, Computer Simulations of Liquids, Clarendon Press, Oxford, 1992.
[45] C.Y. Ng, P.W. Tiedemann, B.H. Mahan, Y.T. Lee, J. Chem. Phys. 66 (1977) 5737.
[46] P.M. Dehmer, S.T. Pratt, J. Chem. Phys. 77 (1982) 4804.
[47] W.R. Wadt, J. Chem. Phys. 68 (1978) 402.
[48] P.M. Dehmer, Comments At. Mol. Phys. 13 (1983) 205.
[49] I. Last, T.F. George, J. Chem. Phys. 93 (1990) 8925.